Fracture characterization of C/C composites under various stress modes by monitoring both mechanical and acoustic responses

A. Bussiba[a,*], M. Kupiec[a], R. Piat[b], T. Böhlke[b]

[a]Nuclear Research Centre Negev, P.O. Box 9001, Beer-Sheva, Israel
[b]Institute of Engineering Mechanics, University of Karlsruhe, Germany

ABSTRACT

C/C composites with different porosities, produced by chemical vapor infiltration have been mechanically tested under quasi-static loading in bending modes using uniform and notched specimens. The acoustic emission (AE) method was used to monitor the damage accumulation profile during loading up to fracture, supported by optical and scanning electron microscope characterization. Three stages in the damage buildup up to fracture were observed: Stage I, with no AE activity, Stage II, gradual growth in AE counts up to an abrupt jump and Stage III, sharp increases in AE counts. Moreover, the similarity in the profile between the cumulative AE counts vs. strain data and the predicted crack density vs. strain by the micro mechanical model suggested for interlaminar cracking, indicates the importance of AE in monitoring the damage evolution in composites in terms of AE counts. Fast Fourier transform analysis of the AE waves revealed three characteristic frequencies in Stage III, which is a sign of three main micro-mechanisms of failure which control the failure progress: fiber fracture, debonding and matrix cracking seem to be the active mechanisms.

1. Introduction

Carbon/carbon (C/C) composites recognized also as carbon fiber reinforced carbon are characterized by their higher specific strength and stiffness of up to 3000 °C in non-oxidizing atmospheres, as compared to other ceramic matrix composites. In addition, the low coefficient of thermal expansion, high thermal conductivity and high thermal shock resistance, have made this material an excellent candidate for aerospace and defence applications for more than three decades. The most popular applications that this unique composite is being used for are: brake discs, rocket nozzles, leading edges of re-entry vehicles, furnace heating, and thermal management components in space vehicles [1].

The severe environmental conditions (mechanical and thermal) which critical engineering structures such as those made of C/C composites have to face, require special attention from manufacturing processes to improve their service in performance [2] aspects. As well-known, defects and flaws may be initiated and may grow as a result of the above conditions and this can upset the mechanical balance of fiber, matrix and interface that gives composites their high performance profile. For the first, the determination of the optimal parametric process, quality control using destructive and non-destructive techniques and mutual properties becomes important. For the second, damage degree development, degradation in performance residual strength, etc., have to be assessed from the structural integrity and life prediction points of view.

Tremendous efforts are being devoted with regard to these important features towards improving the reliability and consistency in using composites, due to their greater complexity and sensitivity over any other engineering media. This activity is being directed towards two different areas but with common goals. One approach has been related to the development of damage models for quasi static [3,4] and fatigue [5,6] loading, usually based on micro-mechanics. Such models predict changes in the stiffness of composite materials due to cracking, and have confirmed the calculated change in the longitudinal Young's modulus due to transverse cracks [7]. More sophisticated models which employ mathematical expressions to describe damage evolution predict changes in the initial material symmetry caused by damage, as well the stiffness changes for all probable crack patterns. The second approach is the application of non-destructive testing techniques for detecting damage and fracture in composite materials. Of these methods, acoustic emission (AE) is the most powerful due to the link between AE data and fracture mechanics parameters, which makes this relation a very useful tool from the engineering viewpoint [8]. In addition, it is possible to monitor the damage accumulation and its profile during loading progress in terms of AE data in real time [9]. Namely, one can distinguish between the well defined three stages of mechanical behavior exhibited in most composites: linear stage (reversible response) which can be characterized by a threshold value (important from the engineering sense), followed by initiation of irreversible damage by different micro-mechanisms of failure but without evidence of macroscopic propagation (can bear increasing loads) and finally, coalescence of damage together with localized micro-cracking growth processes resulting in failure. Moreover, waveform processing of AE signals using fast Fourier transform (FFT), results in frequencies that can point to the various active micro-mechanisms of failure [10]. Extending the analysis using the short-time Fourier transform (STFFT) gives the time information and hence the sequence of the events during fracture process [11].

The current study adopted the AE data to characterize the damage accumulation profile and to specify the operated micro failure modes during loading of two C/C composites with different densities. AE was already used in the early 1960s in monitoring dynamics deformation process in graphite and in composite form. Gilchrist and Wells [12] used this technique to show different acoustic response under stress for graphite composed of isotropic particles (no AE was detected up to just beyond fracture stress) and the other one composed of anisotropic particles which revealed AE long before the final fracture.

More lately, Gareth et al. [13] paid attention to the Felicity effect (AE is detected at stresses less than the previous peak stress) observed at graphites that were subjected to cyclic compressive tensile stresses. This phenomenon was attributed to recovery processes (basal plane shear and microcracking) that occur upon unloading and at zero stress. Recently, Siron et al. [14] characterized the damage and fracture process in correlation with AE waveform parameters of filler-added coal–tar pitch-based C/C composites, under quasi static loading. They concluded that the initiation and propagation of interfiber micro-cracks are ascribed to the low duration and low/medium amplitude events while delamination cracks were associated to medium duration and amplitude and high duration and amplitude related to macrocrack initiation and propagation. The current work ended with a comparison to micro-mechanical model developed for some composites with experimental data obtained by destructive methods with the AE data, is also suggested and discussed.

2. Materials production and microstructure characterization

C/C composites studied in this paper are produced by isothermal, isobaric chemical vapor infiltration. This process for fabrication of C/C materials consists of the synthesis of carbon particles from hydrocarbon gas and their deposition on carbon fibers. The process takes place in a hermetically closed high temperature reactor.

For materials studied in this paper, the process is performed at a temperature of 1095 °C and total pressure of 30 kPa. In this process, the carbon particles deposit in the form of a pyrolytic carbon matrix around the fibers. [15,16]. Fracture surface of the composite exhibit typical layered morphology as presented in Fig. 1 for the low (a) and the high porosity (b).

Carbon fiber felts (CCKF 1001, Sintec, Germany) made of randomly oriented chopped carbon fibers are used as preforms for the infiltration. The fiber volume content is about
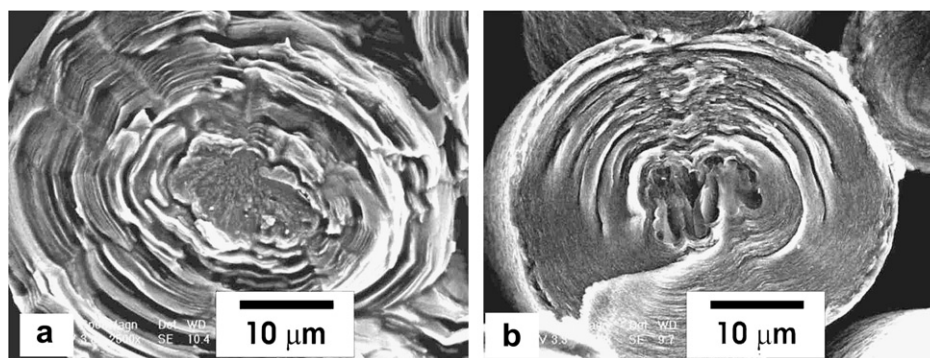

Fig. 1 – Scanning electron microscopy images of the morphology and micro-cracking at the interfaces of the carbon layers in materials with: (a) low porosity and (b) high porosity.

12% (of the total volume) and the diameter of the fibers is of the order of 10 µm. The felts were infiltrated under different conditions (time of infiltration) to obtain matrices with high or low porosity. Infiltration times for the composites were 120 h for low (obtained to be 15%) and 45 h for high porosity (obtained to be 30%). The infiltration was carried out at the Institute for Chemical Technology at the Karlsruhe University in a vertical gap reactor using pure methane as precursor gas. Other details of the infiltration procedure are given in [17,18].

Fig. 2 illustrates the microstructure of the two C/C composites using polarized light microscopy. A general view of the typical microstructure is demonstrated in Fig. 2a. Higher magnification shows the structure of topped cone (Fig. 2b and d) with the fiber at the top surrounded by the carbon matrix. The layered sub-structure of the pyrolytic carbon layers is also noticed in the ring traces at the outer surface of the topped cone (see arrows Fig. 2b and d). It seems that for the

low porous composite those traces are more noticeable as compared to the high porous. Furthermore, the columnar growth is shown (Fig. 2c) in cases where the metallographic cross-section is parallel to the longitudinal axis of the fibers.

3.   Experimental

3.1.   Experimental procedures

Flexural tests were conducted on bars with dimensions of $5 \times 7 \times 55$ mm using three point bending and four point bending (FPB-inner span of 20 mm) set-ups, with outer span of 40 mm (Fig. 3a). A highly sensitive extensometer with maximum scale of 0.5 mm was mounted on a special adapter for measuring the deflection at the outer surface of the specimen. Quasi-static loading with crosshead velocity of 0.5 mm/min was carried out using a computerized servo-
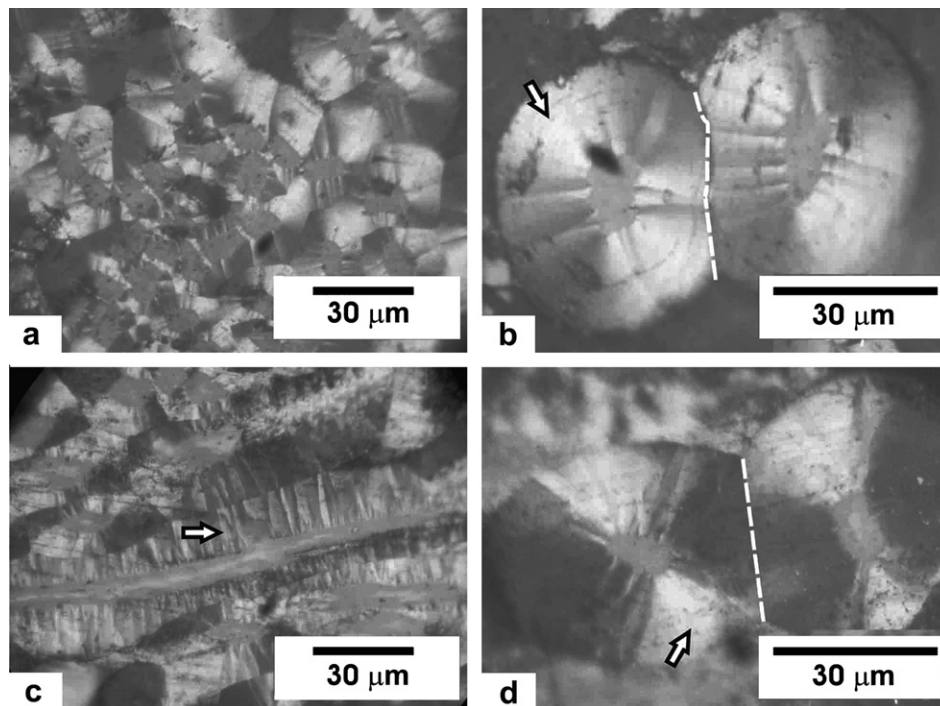

Fig. 2 – Polarized light microscopy micrographs of the microstructures in:(a, b) high porous composite, (c, d) low porous composite (the dashed lines indicate the interface between to fibers surrounded by the matrix).
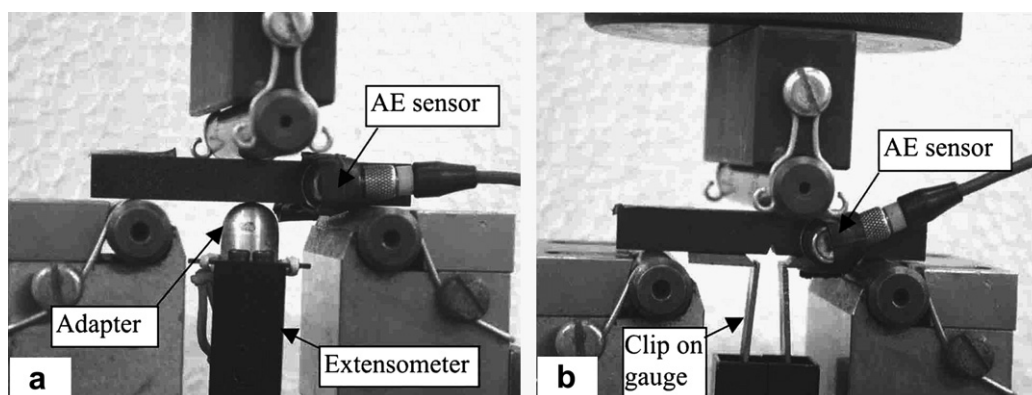

Fig. 3 – Experimental set ups: (a) flexural test of bars and (b) bending of notched bars.

hydraulic machine with a sensitive load cell of 10 kN maximum scale. The flexural properties, modulus, stress and strain at fracture for both configurations were calculated according to the standard expressions for bending beams [19].

Fracture resistance evaluation was determined by means of fracture toughness (K_{IC}), treating the V-notch was as a sharp crack (the radius of the notch was 0.03 mm). Here, only the three point bending set-up was utilized and loading was applied with test velocity of 1 mm/min on notched specimens with dimensions of $4 \times 5 \times 55$ mm and notch depth of 2 mm. Clip on gauge was attached at the front of the notch measuring the crack tip opening displacement (Fig. 3b). The K_{IC} was calculated according to the standard expression for stress intensity factor [20].

$$K_{IC} = \frac{PYS}{BW^{3/2}} \quad \text{with}$$

$$Y = \frac{3\alpha^{1/2}[1.99 - \alpha(1-\alpha)(2.15 - -3.93\alpha + 2.7\alpha^2)]}{2(1+2\alpha)(1-\alpha)^{3/2}} \quad \text{and}$$

$$\alpha = \frac{a}{W}, \tag{1}$$

where P, S, a, W, B and Y are fracture load, span, notch depth, specimen width, thickness and stress intensity shape factor.

On the microscopic scale, the AE technique was used in order to continuously monitor events originating from various sources such as fiber fracture, matrix and interface cracking during the fracture process. So, with the data on fracture sequence events and damage accumulation profile, this method enables us to distinguish between different mechanical responses due to inhomogeneities in the microstructure, such as high and low porosity/micro-cracking/impurities. AE was tracked simultaneously with load and crack opening signals. The AE tests were performed at Gabi Shoef LTD company using computerized AE system MISTRAS 2001 manufactured by PAC. Miniature resonant sensor model 9223M3 with dimension of 9×12 mm (diameter X-height) was used with typical frequency range of 50–600 kHz. Pre-amplification was 60 dB and ambient noise was filtered using a threshold of 30 dB and a 100–1200 kHz bandwidth plug-in filter. In addition, preliminary study was done in order to minimize the AE signals generated from friction (an appropriate lubricant was used) and local damage from stress concentrations at the loading points. A calibration procedure was performed

by loading like composite (graphite/expoxy with high strength) to the critical load range and by placing flexible graphite or grafoil at the loading points. The latter was proved to be good in case of loading sapphire which is very sensitive to burst of twinning at these points at very low load. These actions enable to select the appropriate parameter (gain threshold) while eliminating the undesired AE signals. The sensor was fixed to the specimens using a mechanical device and using silicone grease coupling (see Fig. 3a and b). The AE system allows the processing of a variety of parameters such as counts, energy, rise time, amplitude, and average frequency and so on from the AE waveforms. Preliminary measurements determined the acquisition parameters for the current composite materials (PDT = 50 μs; HDT = 1000 μs; HLT = 300 μs), at a sampling rate of 10 MHz. Ten specimens for each test (flexural and fracture resistance) and for the porosity effect were studied. In addition, AE waveforms were analyzed by applying the FFT function on a majority of the signals in a flexural test on the high porosity composite, for following the majority of the failure mechanisms.

Finally, polarized light microscopy was carried out on polished surfaces in order to track the crack initiation sites, crack profiles and damage features accompanying the main crack, with attention to the porosity. Scanning electron microscopy was performed on the fracture surfaces to characterize and to classify the main failure micro-mechanisms with focus on fracture features of the fibers, micro-cracking in the multilayers, matrix and interface cracking. (see Fig. 2b and d)

3.2. Experimental results

3.2.1. Flexural and acoustic properties

Fig. 4 depicts the mutual responses of two typical low porosity composite specimens which exhibit two different fracture stress (σ_f) levels in terms of AE counts rate (Fig. 4a) and AE cumulative counts (Fig. 4b). As shown, macroscopic linear behavior characterizes this material with very limited elastic strain. In both specimens, the threshold strain (e_{th}) for the onset of AE activity is almost the same with corresponding threshold stress (σ_{th}) as seen in the curves. This AE finding indicates an existing threshold below which no damage is initiated. Siron et al. [14] found also that AE events
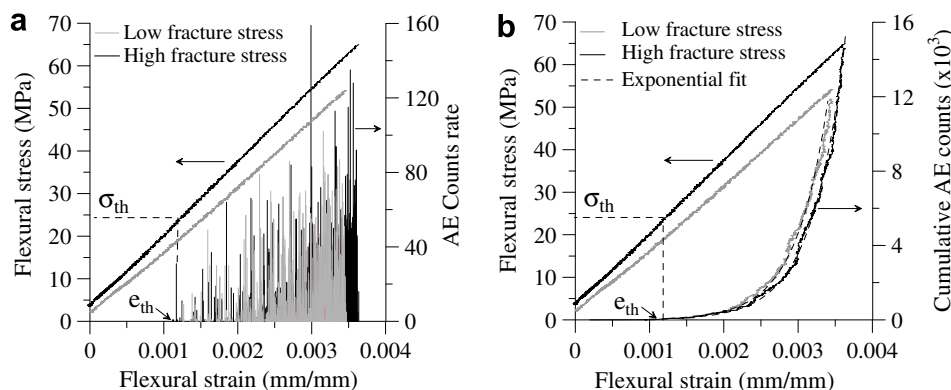

Fig. 4 – Mechanical and acoustic behavior of low porosity for two specimens with different fracture stresses: (a) counts rate and (b) cumulative AE counts.

were detected above a critical strain for unidirectional C/C composites.

Although a similar trend in threshold value is observed, the AE rate obtained for specimen one reached more than 120 counts (Fig. 4a) at the fracture stress, whereas for the second one it was less than 90 (Fig. 4a). This change is reflected in higher fracture stress for the first specimen (66 MPa) as compared to 55 MPa for the second. So, there is a good correlation between the mechanical and acoustic responses, namely higher counts rate resulting in higher fracture stress.

The damage accumulation profile in terms of AE is demonstrated in Fig. 4b by the presentation of cumulative counts. While linear mechanical response is well depicted, an exponential type of contour is obtained for the AE response. So, the damage evolution by AE data in such composites follows the exponential function of the strain. As will be discussed later, this type of AE damage agrees with the exponential curve of the crack density with the strain for some composites.

Fig. 5 illustrates the mutual responses of two typical high porosity composite specimens which show different fracture stress level, in terms of AE counts rate (Fig. 5a) and AE cumulative counts (Fig. 5b). In contrast to the gradual increase in the count rate for the low porosity, here some discrete high count rate is observed from the beginning (Fig. 5a). Due to this irregular behavior, it is difficult to qualitatively predict the fracture stress as in the first case.

Despite this change in the AE response for the high porosity composite, the damage accumulation profile in terms of AE still follows the exponential function (Fig. 5b). So irrespective of the porosity level and the possibility of acceleration or preference of a specific micro-failure due to the change of process parameters, the accumulation of the damage agrees well with the exponential contour.

Fig. 6 presents the different mechanical behaviors of both types of composites in terms of stress and strain along with the AE data. It can be seen in both forms, as count rate (Fig. 6a) and cumulative count (Fig. 6b), that the threshold strain for the onset of AE activity is higher (almost twice) for the low porosity as compared to that for the high porosity. This significant AE finding is important when considering the integrity of the structure during service. The difference in the AE rate and cumulative count is emphasized by the intensification of the damage in the high porosity as compared to that in the low porosity.

Table 1 summarizes the various flexural properties obtained by mechanical testing and two others properties (σ_{th} and σ_{th}/σ_f) acquired by acoustic emission. As expected, increasing porosity level is accompanied by degradation in all the mechanical and acoustic properties. The most influenced parameter is the σ_{th} which decreases significantly, by almost half, for the high porosity composite in comparison to the low porosity composite.
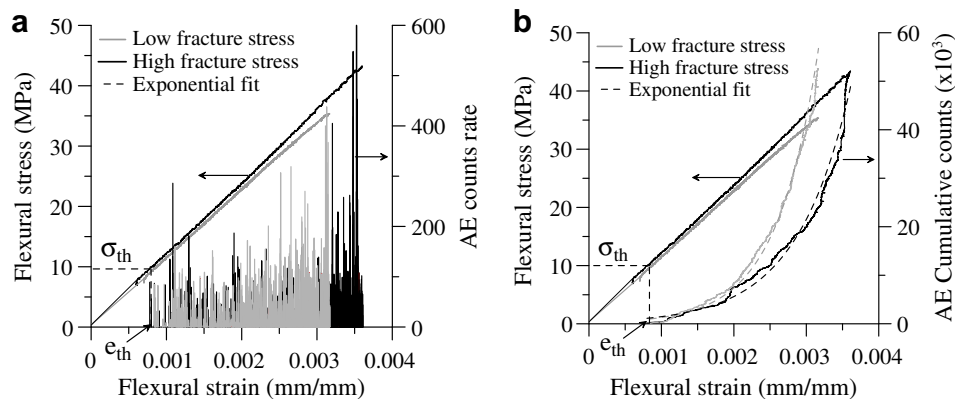

Fig. 5 – Mechanical and acoustic behavior of high porosity for two specimens with different fracture stress: (a) normal AE rate presentation and (b) cumulative AE counts.
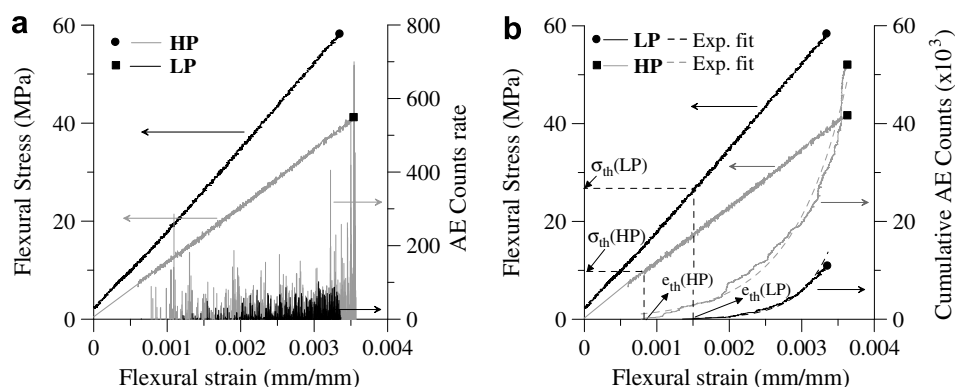

Fig. 6 – Flexural stress and AE vs. flexural strain: (a) counts rate and (b) cumulative counts. LP, low porosity; HP, high porosity.

Table 1 – Flexural and acoustic mechanical properties obtained for both composites

Spec. no.	E (GPa)		σ_f (MPa)		e (×10⁻³) (mm/mm)		$\sigma_{th}{}^b$ (MPa)		$\sigma_{th}/\sigma_f{}^b$	
	Low porosity	High porosity	Low porosity	High porosity	Low porosity	High porosity	Low porosity	High porosity	Low porosity	High porosity
1	16.8	11.8	65	40.4	4	3.4	29.8	10.7	0.45	0.27
2	15.5	12.1	55.5	42.1	3.6	3.5	21.1	9.55	0.38	0.23
3	17.9	13.4	66.5	45.1	3.8	3.35	23.5	13.7	0.36	0.3
4	16.4	12.5	66	37.3	4.0	2.8	20	10.6	0.3	0.28
5[a]		12.2		32.1		3.1				
6[a]		12.7		35.5		3.3				

a Determined by four point bending.
b Defined by acoustic emission data.

Optical microscopy examination of the outer surface of the fractured specimen indicates two main findings in both low porosity and high porosity composites (Fig. 7a and b). (1) The initiated main crack follows the voids (pores) which control its propagation orientation. (2) Each void, which acts as a localized stress concentration, causes micro-cracking and branching phenomena as the main crack passes through it (Fig. 7a and b).

Fig. 8 shows typical failure micro-mechanisms observed near the outer surface of the fractured beam in both composites. In general, for both composites, the main micro-mechanisms can be pointed out: (1) Fracture of fibers surrounded by the carbon multilayers that are parallel or nearly parallel to the loading direction. For the high porosity (Fig. 8a), the result of the incomplete process is reflected in the peeling of the layers due to the weak interfaces. This can be compared to more complete layers with strong interfaces as seen for the low porosity (Fig. 8b). (2) Fracture of the interface, resulting from the intersection of two multilayers, growths (Fig. 2b and d) when the fibers (or the felts) are perpendicular to the loading direction (Fig. 8c). (3) Fracture of the carbon matrix that exhibits low energy fracture surfaces. (Fig. 8d right part of the picture). The characteristic multilayer fracture and the fibers of the low porosity are also depicted in Fig. 8d.

3.2.2. Fracture resistance and acoustic properties

Fig. 9 describes the typical mutual responses of the two notched composites, in terms of AE count rates (Fig. 9a and c) and AE cumulative counts (Fig. 9b and d). As with the case of the uniform stress (in the outer surface), there exists a critical load for the onset of AE activity in both composites. This threshold stress intensity factor, K_{Ith}, is almost half of the low porosity K_{IC} whereas for the high porosity it is only a third of the K_{IC}. The macroscopic deviation from linearity in the load–COD curve is depicted in Fig. 9b and c designated by K_{Ilin}, which indicates an intensification of the AE counts rate resulting from transition in damage accumulation.

This change is accentuated in the high porosity composite (Fig. 9c) where cycle type profile is observed up to the fracture with an increasing amplitude of the sinusoidal wave. Moreover, discontinuities in the load–COD curve are noted with the progress of the fracture process. This type of curve is very similar to quasi-brittle metallic materials that exhibit the pop-in phenomena (abrupt rapid crack growth followed by localized crack arrest). Here, the origin of this mechanism namely, alternating crack growths and arrest events up to fracture, is the presence of pores that act as barriers for the advancing crack. The secondary mechanism is related to crack branching phenomena (see later on), which affects the nominal remote stress intensity factor. These two mechanisms are well suppressed in the low porosity composite and manifested in nearly smooth curves with no indication of macroscopically discontinuous crack growth (Fig. 9a). The AE findings support the mechanical behavior, while the AE count rate increases steeply with the load.

Although a stress–strain gradient is present near the notch tip (in contrast to a "uniform" one as in the case of beam bending), the exponential-type profile of the cumulative AE counts is still preserved up to crack initiation and growth (Fig. 9b and d). A great discrepancy occurs between the
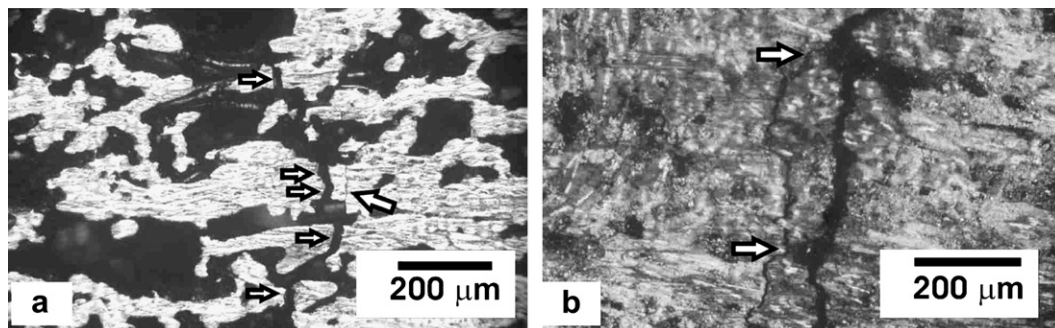

Fig. 7 – Light micrographs of macro- and micro-cracking at the outer surface during flexural test in: (a) high porosity, macro-crack marked by arrows pointed to right and (b) low porosity, micro-cracking and branching indicated by arrows.
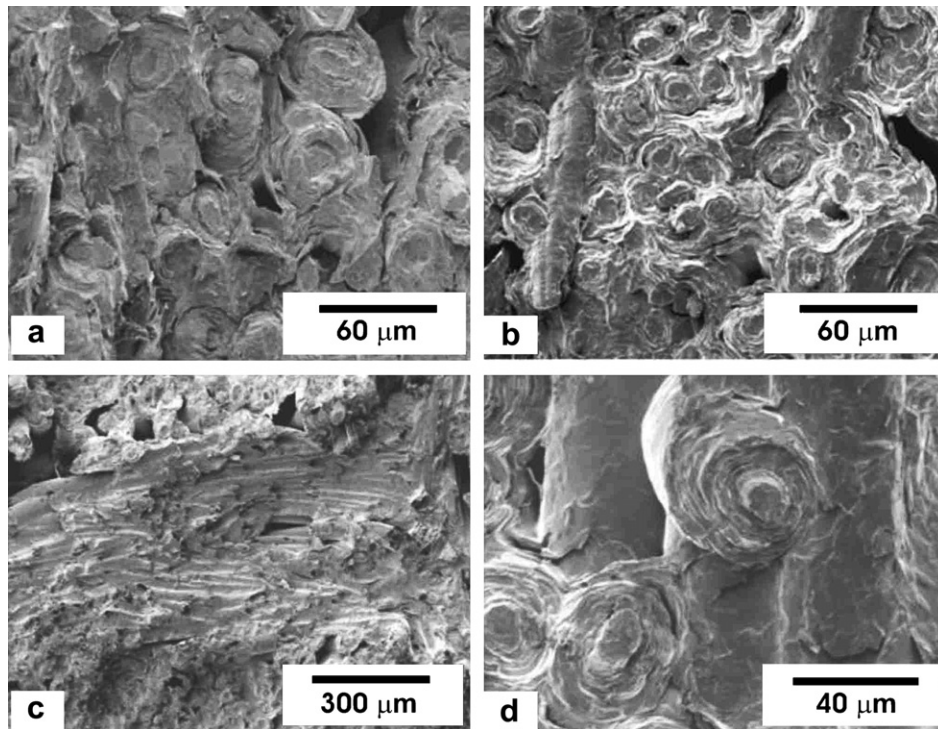
Fig. 8 – Scanning electron microscopy micrographs of failure micro-mechanisms observed in flexural test: (a) fibers and the multilayered in high porosity, (b) fibers and the multilayered in low porosity, (c) fracture of matrix/fibers interface and (d) fracture of the multilayered matrix.
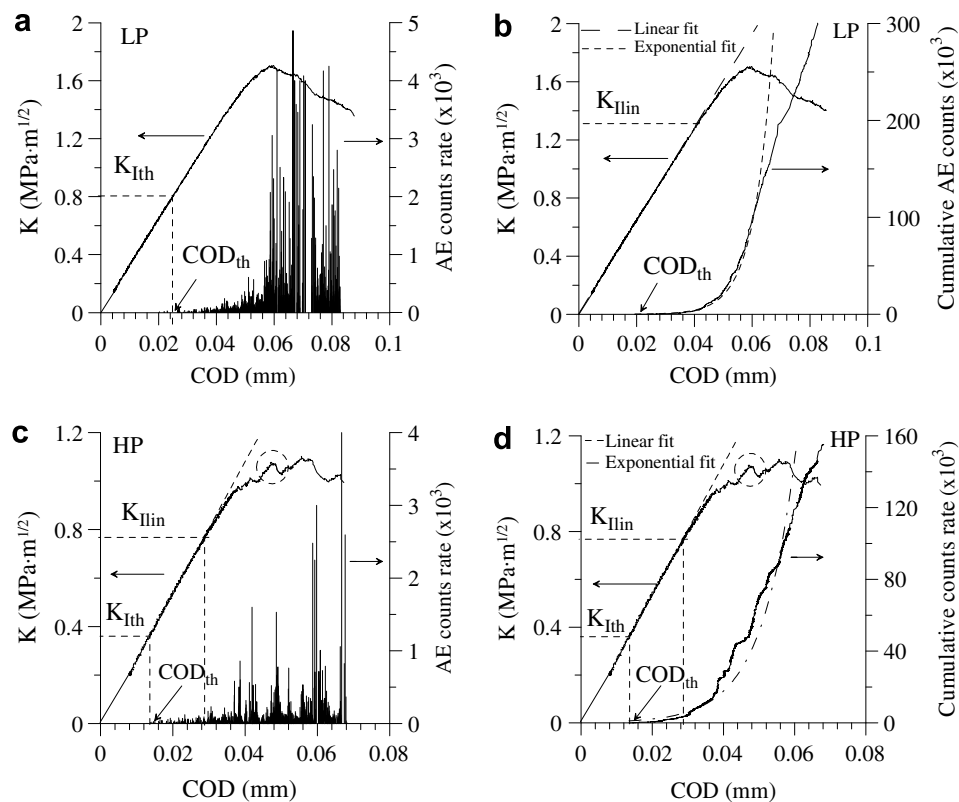

Fig. 9 – Load, acoustic emission rate (a, c) and cumulative (b, d) vs. crack opening displacement for the low porosity and high porosity composites.

Spec. no	K_{IC} MPa m$^{1/2}$		K_{Ith} MPa m$^{1/2}$		$K_{ILin.}$ MPa m$^{1/2}$		K_{Ith}/K_{IC}	
	Low porosity	High porosity	Low porosity	High porosity	Low porosity	High porosity	Low porosity	High porosity
1	1.66	0.84						
2	1.35	0.97		0.36				
3	1.6	1.02	0.74	0.35		0.68	0.46	0.36
4	1.76		0.74		1.4	0.55	0.42	0.35

Table 2 – Fracture toughness and threshold values for both composites

exponential fit and the actual curve from the point of crack growth up to the point of unstable crack growth. Actually, the exponential behavior is also observed in each cycle of discontinuous crack growth (see dashed circle in Fig. 9c).

Table 2 summarizes the fracture toughness, K_{IC}, results for both composites. The decrease in fracture resistance with increasing porosity is well documented. The two additional parameters and a normalized one acquired by acoustic emission, are also given; K_{Ith} (first detection of AE counts), K_{Ilin} (a dominant change in the AE count rate – see later) and K_{Ith}/K_{IC}. The same trend of degradation as that seen in K_{IC} is also observed for the mechanical parameters characterized by AE (K_{Ith} and K_{Ilin}).

Fig. 10 points to the crack profile during crack growth in notched low porosity and high porosity specimens. As shown the crack was initiated at a pore near the root of the notch (Fig. 10a and c), which reveals the influence of the pores on the stress field near the crack tip. Any disturbance near the crack vicinity may affect the crack initiation site as well the crack orientation. As in the case of the uniform stress, the crack follows the pores, which cause an irregularity in the crack path. In addition, crack branching (Fig. 10b) occurs

due to pores and micro-cracking accompanying the main crack that passes through the pores (Fig. 10d).

Finally, Fig. 11 illustrates characteristic fracture modes for both composites. Fig. 11a and b emphasize the fracture of the fibers near the notch tip with an enhancement of multilayered micro-cracking (Fig. 11b) in high porosity. The fracture of the fibers and the matrix cracking with low energy fracture surface for the low porosity are shown in Fig. 11c and d, respectively.

Beyond the illustration of damage process at the macroscopic level, AE gives some insights on the local failure mechanisms. Following the AE events analysis suggested by Siron et al. [14] for C/C composite, Fig. 12 depicts an illustration of test time, amplitude and duration of the events recorded during loading up to fracture of high porosity uniform bend specimen.

The amplitude events can be distributed to three ranges: 30–45, 45–70 and 75–95 dB (Fig. 12a) while the correlation of amplitude with duration is shown in Fig. 12b. The stress profile with test time is given in Fig. 12c. The low range amplitude is accompanied by low duration (<500 μs) up to stress of 22 MPa equivalent to 20 s of test time. The medium range is
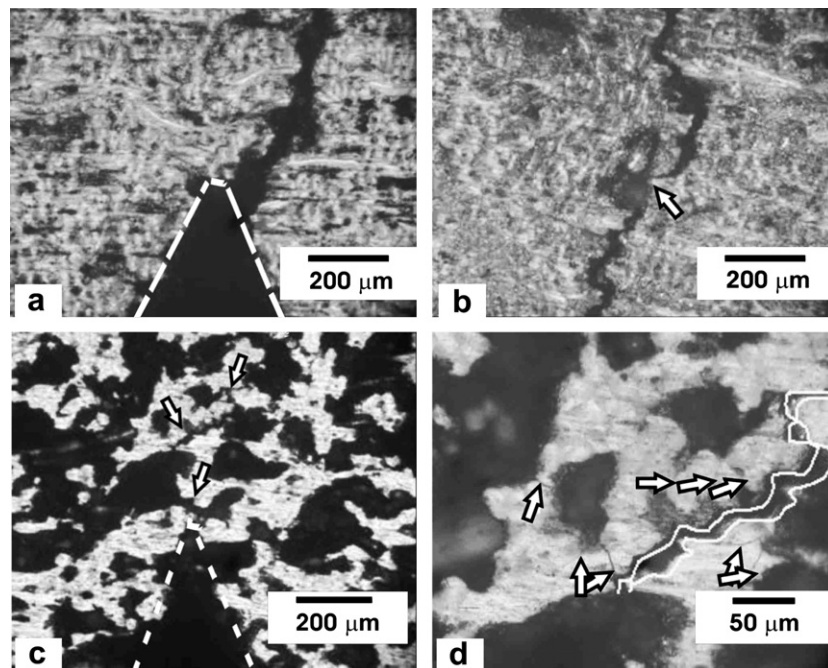

Fig. 10 – Polarized light microscopy images with crack path and damage features accompanying the crack growth: (a) crack initiation site in low porosity, (b) crack branching in low porosity, (c) crack initiation site in high porosity and (d) cracking in the vicinity of the main crack.
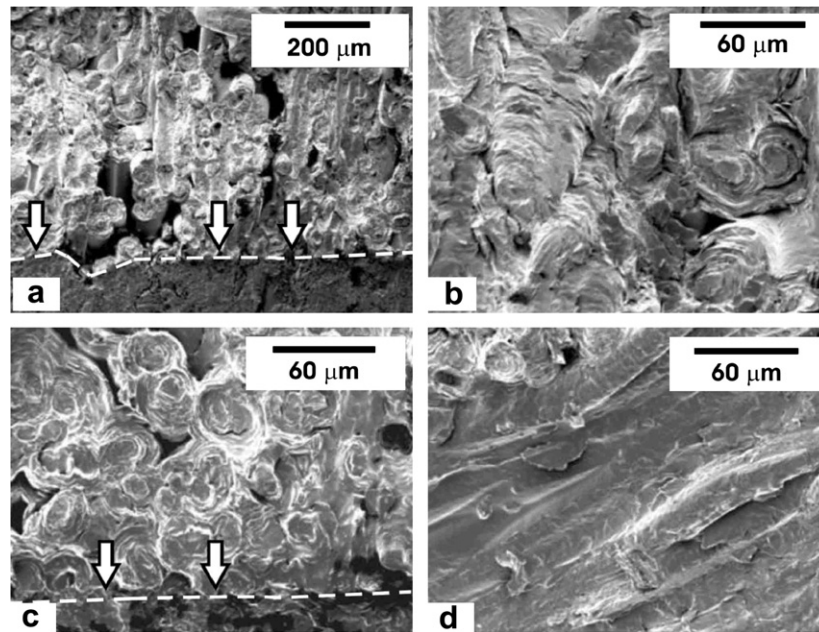
Fig. 11 – Scanning electron microscopy images of the main fracture modes developed during crack growth in (a) fibers break near notch tip in high porosity, (b) micro-cracking at the multilayers, (c) fibers break near notch tip in low porosity and (d) matrix cracking.
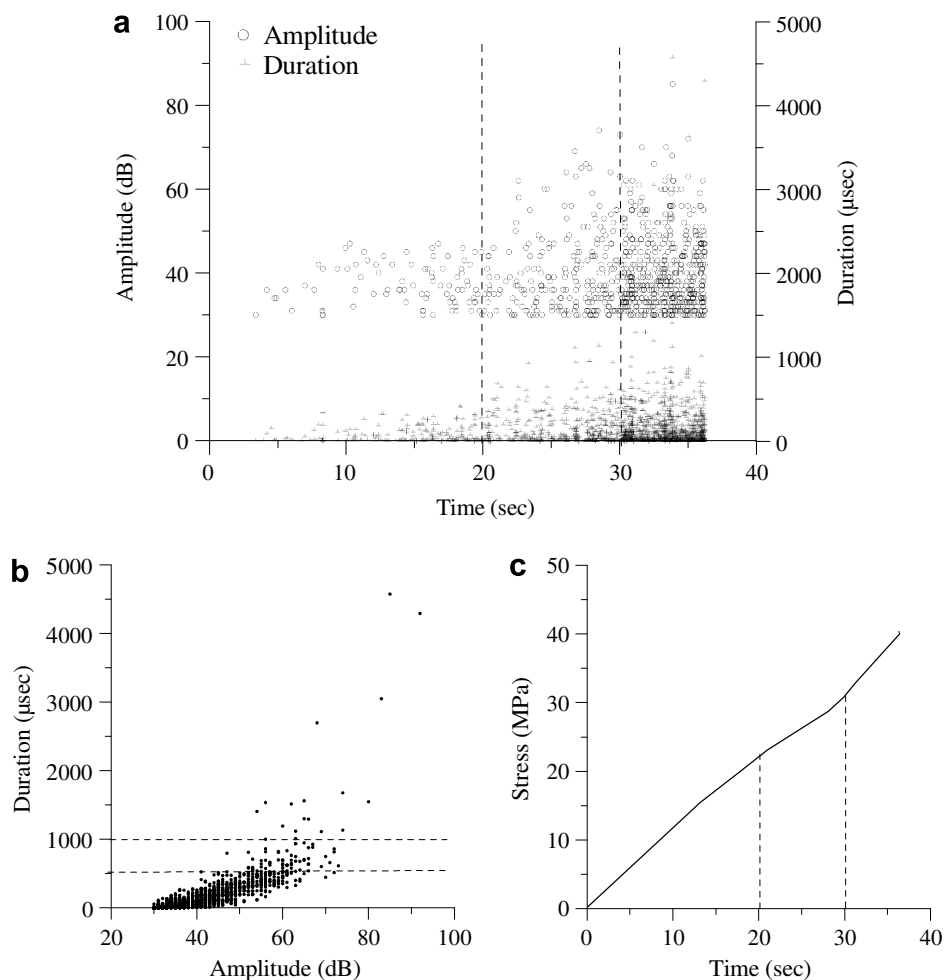

Fig. 12 – (a) Amplitude and duration vs. test time obtained during loading of high porosity bend specimen, (b) duration vs. amplitude and (c) load vs. time.

associated with increasing in duration time of the events (500–1000 μs) up to stress of 32 MPa. The high range is related to a sharp increase in the duration time (1000–4500 μs) up to the final fracture. Based on the fracture surface study and in corresponding to Siron et al. [14] one can assume that three basic failure modes control the fracture of such composite as related to the mentioned order ranges of amplitude and duration: micro-cracking of the multilayered matrix, fiber fail-ure (bundle failure) and initiation and propagation of macro-cracks.

By applying the FFT function for some AE waveforms in the ranges mentioned above some correlation was noticed. The most common profile in the frequency domain that was detected during the scan of the AE waves in the high ampli-tude range is illustrated in Fig. 13b and the corresponding wave is given in Fig. 13a. As shown, three main characteristic
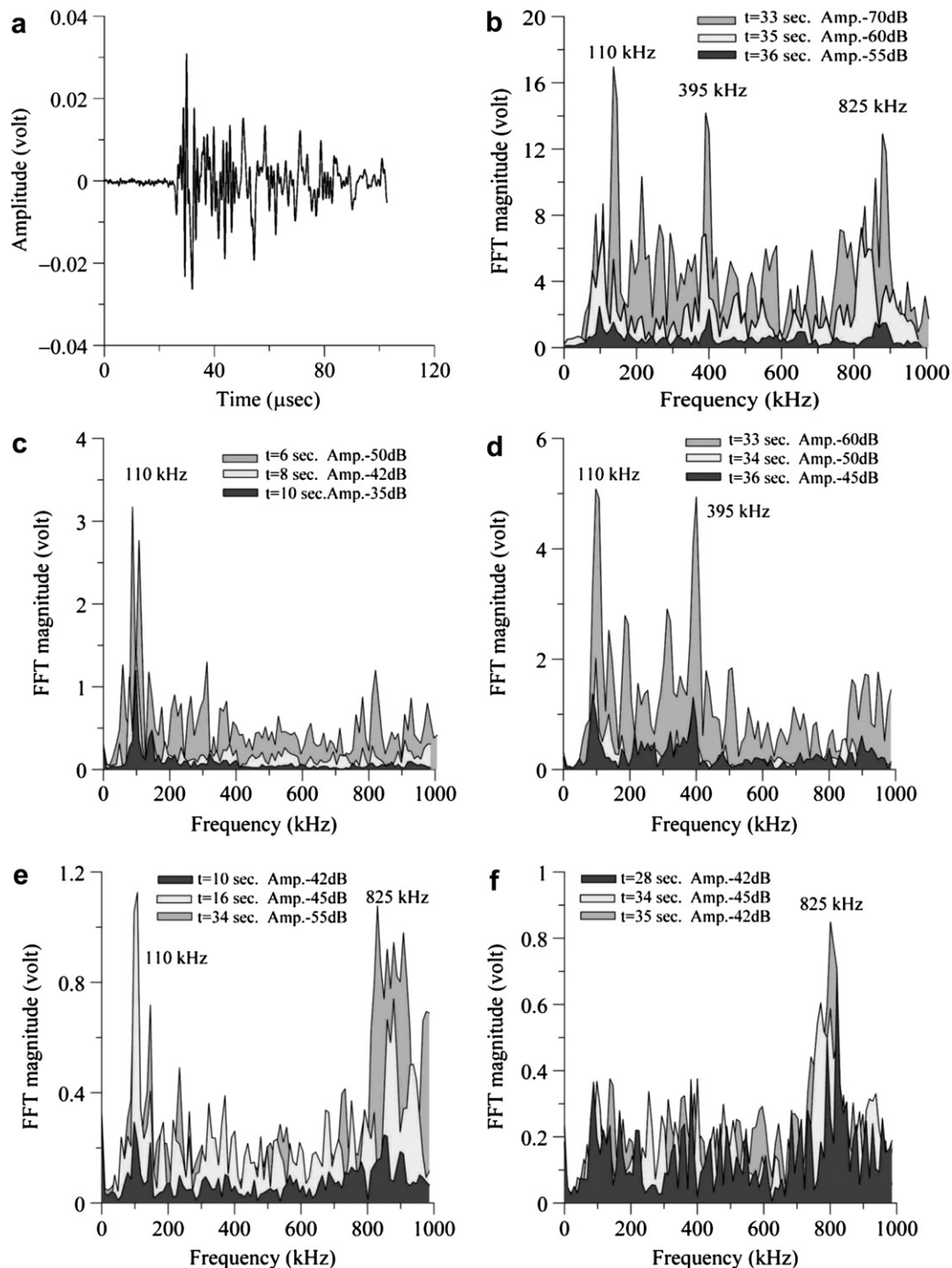

Fig. 13 – The AE wave and the frequency domain at different times and amplitudes of the signal, (a) AE wave, (b) corresponding FFT with the three frequencies, (c) low ƒ, (d) low and medium ƒ, (e) low and high ƒ and (f) high ƒ.

frequencies were observed, one in the range of 110–140 kHz, the second in the range of 370–395 kHz and the last one in the range of 830–890 kHz. It can therefore be assumed that three dominant micro-mechanisms controlled the fracture process of this composite as also claimed above. For nearly 13 s of the test time (low amplitude range), only the low characteristic frequency was noticed (Fig. 13c) which maybe related to the cracking of the multilayered matrix. Combination of low and medium frequencies (Fig. 13d) in the medium amplitude range was detected, which indicates additional active micro-failure mechanism that maybe the fiber failure (bundle failure). The high frequency alone was less common (Fig. 13f) and can be associated to initiation and propagation of macro-cracks. Another combination of frequencies is also given in Fig. 13e. More work has to be done in order to correlate in more detailes the actual micro-mechanisms as well as the sequence of fracture with the corresponding characteristic frequencies. Such investigations are presented by Ni et al. on carbon fiber reinforced carbon composites [11]. In addition, artificial intelligence techniques such as, partitional clustering analysis [21] or unsupervised pattern recognition [22] are being used for the classification of AE events and thereby discrimination between various failure mechanisms.

4.   Discussion

The AE data generated in both stress fields (uniform and localized) along with the mechanical response, highlight the mode of the damage accumulation profile in the C/C composite for both densities. As shown, the macroscopic linear elastic behavior of the load versus displacement is accompanied by exponential-type profile of the cumulative AE counts irrespective of the density degree. This type of AE features accumulation was also reported by Siron et al. [14] on unidirectional C/C composites for the 90° off-axis tensile tests, as well as by Gareth et al. [13] in polygranular graphite IMI-24 (spherical particles with coal–tar pitch binder) subjected to compressive load. As mentioned, the three stages of the damage progress are well reflected in the AE curve. The first one is ended by the threshold strain (or alternatively by the threshold COD in the case of a notched specimen) as observed in other composite materials [9,23]. Here, no AE activity is noticed, thus a reversible behavior without damage characterized this part of loading. The second stage can be determined either by a significant jump in the cumulative AE counts or by intersection between the nearly linear behavior at the early stage of loading and the exponential-type behavior with further loading. Fig. 14 illustrates both of the above-mentioned cases for uniform and notched bars. Fig. 14a and c clearly show the transition from stage two to stage three separated by the significant localized jump at the cumulative AE counts (bounded by two small arrows) for high porosity in the uniform and notched bars, respectively. Looking carefully at Fig. 14c reveals that the abrupt increase in the AE counts is accompanied by a deviation from linearity in the load–COD curve, less seen for low porosity in the uniform (Fig. 14b) and notched bars (Fig. 14d) where smooth curves are obtained. As noted, the end of stage two
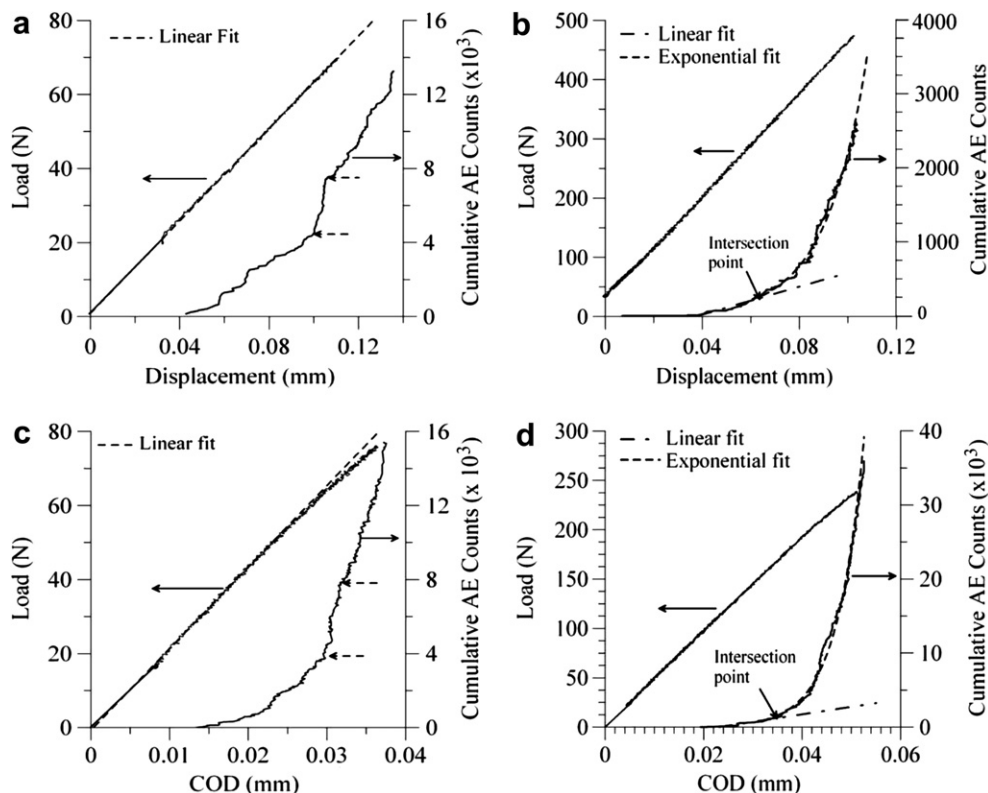

Fig. 14 – The transition from stage two to stage three in uniform bar for: (a) high porosity, (b) low porosity and for notched bar, (c) high porosity and (d) low porosity.
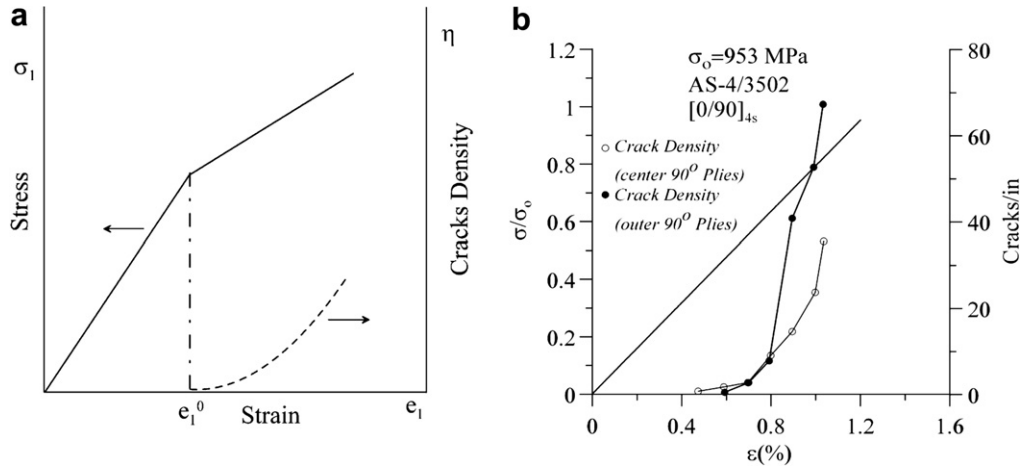
Fig. 15 – (a) A bilinear stress–strain behavior with associated transverse crack density and (b) experimental stress–strain curve and associated transverse crack density of a graphite–epoxy (0,90) [25].

corresponds to $K_{ILin.}$ given in Table 2. Stage three, which involved coalescence of damage and macroscopic crack growth, is characterized by a discontinuous curve of both the AE and the load with the COD. So, the three stages of damage evolution were identified with mechanical parameters that indicate the transition between them.

In to the micro-mechanical model suggested by Talreja [3], for interlaminar cracking in composite laminates he obtained an expression for the damage tensor of such cracking as

$$D_{ij} = \frac{k t_c^2}{s t \cos \theta} n_i n_j, \qquad (2)$$

where t is the thickness of the element, t_c is the ply thickness, s the crack spacing, θ the angle between the fiber direction and the transverse direction and $n = (\cos \theta, \sin \theta, 0)$.

Using a thermodynamic framework for description of material response, he determined the damage D_1 for a bilinear stress–strain curve in the following form:

$$\log \frac{D_1}{D_1^0} = \frac{E_t}{\eta} \left[d_4 (e_1 - e_1^0) + A \left\{ e_1^2 - \left(e_1^0 \right)^2 \right\} + B \left\{ e_1^3 - \left(e_1^0 \right)^3 \right\} \right], \qquad (3)$$

where D_1^0 is the initial damage (initial crack density) that begins to grow at threshold strain e_1^0 and E_t the tangent modulus beyond the initiation of damage growth. Combining Eq. (2) for the non-zero component of damage tensor and Eq. (3) with $\eta = 1/s$, gives the result that the crack density is an exponential function of the strain, as shown schematically in Fig. 15a dashed curve (more details are given in the above reference). The predicted profile is in agreement with experimental results obtained by Kistner et al. [24] in graphite–epoxy as illustrated in Fig. 15b. The exponential behavior of the crack density vs. strain was also viewed in NCF cross-ply laminates up to the transition point where damage coalescence is operating [25]. As shown, the AE results, in terms of cumulative counts, exhibit an exponential behavior of the strain or the COD (up to the point of macroscopic crack growth). Moreover, the AE data confirm the existence of a threshold strain which is also pointed out by the model. So, the likeness between the AE data and the model supported by experimental results indicates the power of AE in monitoring the damage evolution profile in composites. In addition, it

is very useful in determining the dependency of the crack density on the strain in cases where counting the cracks is an impossible operation as in our case.

5. Summary and conclusions

The current C/C composites were fabricated by isobaric chemical vapor infiltration of carbon fiber felts with two different porosities (15% and 30%) resulting from different processing histories. Both composites were characterized mechanically by means of a flexural test in a three point bending set-up of uniform and notched beams. Flexural properties including elastic modulus and fracture resistance property in terms of fracture toughness were determined. In situ AE was monitored simultaneously during loading up to fracture. The collected AE signals were analyzed and correlated to the mechanical response. Metallographic examination of the damage features along the crack path and fractographic study of the fracture modes support the mechanical and acoustic findings.

With these, the following are concluded:

1. Increasing the porosity is accompanied by degradation in the entire mechanical and acoustic properties. The threshold stress corresponding to the threshold strain (determined by AE data) decreases significantly by almost half for the high porosity composite as compared to the low porosity composite.
2. There is a good correlation between the mechanical and acoustic responses, namely higher AE counts rate resulted in higher fracture stress.
3. Damage evolution characterization by AE data follows an exponential function of strain, despite its linear macroscopic elastic mechanical response. These mechanical and AE behaviors are independent of the porosity degree.
4. The crack initiation site and its orientation are influenced by the existence of the pores near the root of the notch as well as at the outer surface of the beam. The crack follows the pores which cause an irregularity in the crack path and lead to the development of crack branching.

5. Increasing porosity causes decrease in fracture resistance, K_{IC} as well as in both mechanical K_{Ith} and K_{ILin} acquired by AE data.

6. The exponential type profile of the cumulative AE counts is still preserved up to crack initiation point in case of sharp stress–strain gradient, which exists in the vicinity of the notch tip.

7. The well-known three stages of damage evolution in composites were identified by the AE activity. In stage I no AE events were recorded up to the threshold strain. In stage II moderate increase of the cumulative AE counts (tend to be linear) was observed up to an abrupt jump in this parameter, and from this point up to fracture, stage III is controlled by the damage growth. Beyond this, it also highlights the mechanism of damage evolution from discrete events (Stage II) to a more continuous one (Stage III).

8. The similarity in the profile between the cumulative AE counts vs. strain data and the predicted crack density vs. strain by the micro-mechanical model, suggested for interlaminar cracking, supported by experimental results indicates the power of the AE in monitoring the damage evolution in composites in terms of counts.

Acknowledgements

R E F E R E N C E S

[1] Manocha LM. High performance carbon–carbon composites. Sadhana 2003;28(1–2):349–58.

[2] Huguet S, Godin N, Gaertner R, Salomon L, Villard V. Unsupervised clustering techniques for the characterization of failure modes in GFRP composite by acoustic emission. ECF13, San Sebastián, 6-9.09.2000.

[3] Talreja R. Continuum modeling of the development of interlaminar cracking in composite laminates. In: Extended abstracts, Proc of the 7th int conf on fracture, Houston, TX; 1989. p. 2191–9.

[4] Hashin Z. Analysis of orthogonally cracked laminates under tension. J Appl Mech 1985;54(4):121–36.

[5] Akshantala NV, Talreja R. A micromechanics based model for predicting fatigue life of composites laminates. Mater Sci Eng A 2000;285:303–13.

[6] Akshantala NV, Talreja R. A mechanistic model for fatigue damage evolution in composite laminates. Mech Mater 1998;29(7):123–40.

[7] Bouazza M, Tounsi A, Benzair A, Adda-Bedia EA. Effect of transverse cracking on stiffness reduction of hygrothermal aged cross-ply laminates. Mater Design 2007;28(4):1116–23.

[8] Huang M, Jiang L, Liaw PK, Brooks CR, Seeley R, Klarstrom DL. Using acoustic emission in fatigue and fracture materials research. J Miner Met Mater Soc 1998;50(11):66. Available from: ⟨http://www.tms.org/pubs/journals/JOM/9811/Huang/Huang-9811.html⟩.

[9] English LK. Listen and learn: AE testing of composites. Mater Eng, ADD441501; 1987.

[10] Woo SC, Choi NS. Analysis of fracture process in single-edge-notched laminated composites based on the high amplitude acoustic emission events. Compos Sci Technol 2007;67(7–8):1451–8.

[11] Ni QQ, Kurashiki K, Iwamoto M. AE technique for Identification of micro failure modes in CFRP composites. Mater Sci Res Int 2001;7(1):67–71.

[12] Gilchrist KE, Wells D. Acoustic emission from graphite under stress. Carbon 1968;6(2):627–31.

[13] Gareth BN, McEnaney B. Creep and recovery in graphite at ambient temperature: an acoustic emission study. Carbon 1994;32(4):553–8.

[14] Siron O, Chollon G, Tsuda H, Yamauchi H, Maeda, Kosaka K. Microstructural and mechanical properties of filler-added coal–tar pitch-based C/C composites: the damage and fracture process in correlation with AE waveform parameters. Carbon 2000;38(9):1369–89.

[15] Reznik B, Hüttinger KJ. On the terminology for pyrolytic carbon. Carbon 2002;40(4):621–4.

[16] Reznik B, Gerthsen D, Hüttinger KJ. Macro- and nanostructure of the carbon matrix of infiltrated carbon fiber felts. Carbon 2001;39(2):215–29.

[17] Benzinger W, Hüttinger KJ. Chemistry and kinetics of chemical vapour infiltration of pyrocarbon-V. Infiltration of carbon fiber felt. Carbon 1999;37(6):941–6.

[18] Benzinger W, Hüttinger KJ. Chemistry and kinetics of chemical vapor infiltration of pyrocarbon-VI. Mechanical and structural properties of infiltrated carbon fiber felt. Carbon 1999;37(6):1311–22.

[19] ASTM D790-95a – standard test methods for flexural properties of unreinforced and reinforced plastics and electrical insulating materials; 1996. p. 155.

[20] ASTM E399-90 (Reapproved) – standard test method for plane-strain fracture toughness of metallic materials; 2005. p. 462.

[21] Anastassopoulos AA, Philippidis TP. Clustering methodology for the evaluation of acoustic emission from composites. J Ac Emiss 1995;13(1–2):11–22.

[22] Anastassopoulos AA, Philippidis TP, Paipetis SA. Failure mechanism identification in composite materials by means of acoustic emission: Is it possible? In: van Hempelrijck, Anastassopoulos AA, editors. Non destructive testing. Rotterdam: Balkema; 1996. p. 143–9.

[23] Bourchak M, Farrow IR, Bond IP, Rowland CW, Menan F. Acoustic emission energy as a fatigue damage parameter for CFRP composites. Int J Fatigue 2007;29(3):457–70.

[24] Kistner MD, Whitney JM, Browning CE. First ply failure of graphite/epoxy laminates. In: Recent advances in composites in the Unites States and Japan, vol. 864. ASTM STP; 1981. p. 44–61.

[25] Edgren F, Mattsson D, Asp LE, Varna J. Formation of damage and its effects on non-crimp fabric reinforced composites loaded in tension. Comput Sci Technol 2004;64(5):675–92.